Geophysical Research Letters

RESEARCH LETTER
10.1029/2024GL113995

Special Collection:
Science from the Surface Water and Ocean Topography Satellite Mission

A Practical Separation of Oceanic Vortical and Wavy Motions Entangled in the SWOT Measurements

Chuanyin Wang[1], Zhiyu Liu[2], Hongyang Lin[2], Dake Chen[1,3], Qinghua Yang[1,4], and Qinbiao Ni[1]

[1]Southern Marine Science and Engineering Guangdong Laboratory (Zhuhai), Zhuhai, China, [2]State Key Laboratory of Marine Environmental Science, and Department of Physical Oceanography, College of Ocean and Earth Sciences, Xiamen University, Xiamen, China, [3]State Key Laboratory of Satellite Ocean Environment Dynamics, Second Institute of Oceanography, Ministry of Natural Resources, Hangzhou, China, [4]School of Atmospheric Sciences, Sun Yat-sen University, Zhuhai, China

Abstract The recently launched Surface Water and Ocean Topography (SWOT) satellite provides an unprecedented two-dimensional measurement of the sea surface height (SSH) down to the oceanic submesoscale of 1–10 km. Using this measurement to make substantial progress requires the separation of vortical and wavy motions owing to their contrasting ramifications for the energy transfer; however, the separation is extremely challenging due to the long-repeat period of the SWOT satellite. To achieve a practical separation, here we adopt the linear normal-mode initialization technique used in numerical weather prediction. This separation method requires velocity data in addition to SSH. With concurrent measurements of SSH and velocity respectively from SWOT and the offshore high-frequency radar (HFR) system, this separation method proves valid and useful. The present study is expected to stimulate new discoveries associated with oceanic multiscale interactions and energy transfers.

Plain Language Summary The Surface Water and Ocean Topography (SWOT) satellite measures a wide area of the sea surface height. These measurements contain two types of oceanic motions. One is the vortical motion generally including the mesoscale flow and submesoscale processes. The other is the wavy motion mainly incorporating the (internal) inertial-gravity wave. In SWOT measurements, one type of motion could hide the other. For example, the wavy (vortical) signal might become invisible in the oceanic region characterized by the intense vortical (wavy) motion. This raises the need to separate the two types of motions from SWOT measurements, which remains a major challenge due to their overlap in horizontal scales. To this end, this study uses the initialization technique in numerical weather prediction and realizes a practical vortical-wavy separation of SWOT measurements via additionally introducing concurrent sea surface velocity data from the land-based HFR system. The applications highlight the validity and usefulness of this separation approach.

Key Points:

- A dynamics-based method is used to conduct a practical separation of vortical and wavy motions in Surface Water and Ocean Topography measurements
- This separation method is based on the linear normal-mode initialization technique used in numerical weather prediction

Supporting Information:

Supporting Information may be found in the online version of this article.

Correspondence to:

Z. Liu,
zyliu@xmu.edu.cn

Citation:

Wang, C., Liu, Z., Lin, H., Chen, D., Yang, Q., & Ni, Q. (2025). A practical separation of oceanic vortical and wavy motions entangled in the SWOT measurements. *Geophysical Research Letters*, *52*, e2024GL113995. https://doi.org/10.1029/2024GL113995

Received 29 NOV 2024
Accepted 28 MAY 2025

Author Contributions:

Conceptualization: Chuanyin Wang, Zhiyu Liu
Formal analysis: Chuanyin Wang
Funding acquisition: Zhiyu Liu
Investigation: Chuanyin Wang
Methodology: Chuanyin Wang, Zhiyu Liu
Project administration: Zhiyu Liu
Resources: Zhiyu Liu
Supervision: Zhiyu Liu
Visualization: Chuanyin Wang
Writing – original draft: Chuanyin Wang

1. Introduction

The Surface Water and Ocean Topography (SWOT) satellite, launched in December 2022, provides the first two-dimensional measurement of sea surface height (SSH) with an unprecedented spatial resolution of O(10 km) (Fu et al., 2024). Compared with the conventional nadir-looking altimetry, the SWOT satellite has the unique advantage of accurately measuring barotropic tides in complex coastal regions (Hart-Davis et al., 2024), internal gravity waves (Archer et al., 2025; Qiu et al., 2024) and submesoscale processes (Archer et al., 2025; Zhang et al., 2024). As a result, the measured SSH by SWOT contains combined contributions of vortical (including large-scale circulations, mesoscale eddies and submesoscale currents) and wavy (including barotropic tides and internal gravity waves) motions. It is of necessity to separate vortical and wavy motions due to their contrasting impact on oceanic energy transfer and turbulent mixing (Klein et al., 2019); a proper removal of wavy signals is also necessary to achieve an accurate estimation of geostrophic velocities from the SWOT measured SSH (Morrow et al., 2023). However, such a separation is very challenging owing to the long-repeat period (i.e., 1 day during the CalVal phase and 21 days during the science phase) of the SWOT satellite which inadequately captures the temporal evolution of submesoscale currents and internal gravity waves (Klein et al., 2019; Le Guillou et al., 2021; Morrow et al., 2019).

Several attempts have been made to address this challenge. One is to exploit the temporal aliasing caused by the long-repeat period to recover coherent internal tides. This approach has long been applied to conventional, nadir-

Writing – review & editing: Zhiyu Liu, Hongyang Lin, Dake Chen, Qinghua Yang, Qinbiao Ni

looking satellite altimetric data (Carrère et al., 2004; Dushaw, 2015; Kantha & Tierney, 1997; Ray & Mitchum, 1996; Ray & Zaron, 2016; Zaron, 2019; Zhao, 2017; Zhao et al., 2016) and was recently applied to SWOT measurements (Tchilibou et al., 2024). However, this approach does not apply to the extraction of incoherent internal tides and internal gravity waves at non-tidal frequencies. Another approach, which only works for the summertime, employs the spatial filtering to separate vortical and wavy SSH with the cutoff chosen as the slope discontinuity of SSH wavenumber spectra (H. S. Torres et al., 2019). An additional approach is through assimilating SWOT measured SSH into the numerical ocean model, the output of which is then used to separate vortical and wavy motions. Le Guillou et al. (2021) and Yadidya et al. (2024) provide preliminary application examples. More advanced techniques are required to tackle the difficulty of directly assimilating SWOT SSH which has multiscale characteristics. The machine learning also proves useful (Gao et al., 2024; Lguensat et al., 2020; H. Wang et al., 2022); nevertheless, its applicability to SWOT measurements remains unknown.

Here we hightlight that the initialization technique in numerical weather prediction can inspire a more general and accurate vortical-wavy separation that is applicable to SWOT measurements. In the history of weather prediction using primitive equations models, there exists a long-standing effort to reduce or arrest the growth of meteorologically-unimportant internal gravity waves via defining a balance between the initial pressure and velocity fields (e.g., Coiffier, 2011). An adequately successful attempt is the linear normal-mode initialization (Dickinson & Williamson, 1972; Williamson, 1976). Building on the fact that vortical and wavy modes are eigenfunctions of the linearized governing equations, this initialization filters out internal gravity waves via directly setting the wavy mode in the initial fields to be zero. This filtering is exactly consistent with the fundamental property that wavy motions do not induce any potential vorticity (PV) anomaly relative to the rest state (Pedlosky, 2003; Zeitlin, 2018). For this reason, this initialization technique is called the PV-based method in this study. Recently, C. Wang et al. (2025) formulated the PV-based method in the rotating shallow water system and made a proof-of-concept application to a concurrent snapshot (i.e., $\sim 5^\circ \times 5^\circ$ box) of sea surface height and velocity (SSV) extracted from a high-resolution numerical simulation. They show that the PV-based method is capable of achieving a satisfactory vortical-wavy separation in contrasting dynamical regimes (i.e., the South China Sea with strong internal tides but weak eddy activities and the Kuroshio Extension with strong eddy activities but weak internal tides). As a follow-up, this study applies the PV-based method to SWOT measurements of the real ocean.

For realistic application, the SSV measurement concurrent with SWOT SSH is required. At the present time, this requirement is feasible for many parts of the coastal oceans where SSV from the high-frequency radar (HFR) system is available on SWOT swaths. The HFR data have shown an encouraging capability in capturing submesoscale processes (Chavanne et al., 2010; Lai et al., 2017; Payandeh et al., 2023; Soh & Kim, 2018; Yoo et al., 2018) and internal tides (Kachelein et al., 2024; Lee & Kim, 2022). Here we choose the offshore region of California, which is well supported with a HFR network, to test the PV-based method. We will proceed in two steps. Firstly, SSH and SSV from a realistic tide-resolving and submesoscale-admiting numerical simulation (i.e., MITgcm LLC4320) are regridded onto the swath-style grid of SWOT to mimic the real-ocean observations; then the PV-based method is applied to the regridded SSH and SSV and is validated against the baseline separation that will be described in Section 2.2. Secondly, the SWOT measured SSH and HFR measured SSV are remapped onto the SWOT grid and then vortical and wavy motions are separated.

2. Materials and Methods

2.1. SSH and SSV Data

The SWOT satellite observes SSH over two parallel 50-km swaths interleaved with a 20-km nadir gap. The horizontal resolution of the SWOT SSH product, namely SWOT Level-3 (L3) SSH Expert, is 2 km over each swath. The HFR system routinely provides a two-dimensional measurement of SSV with a horizontal resolution of 6 km. In this study, we select an oceanic region (i.e., 35°–40°N, 235°–240°E) offshore of California since this region is well covered by the HFR system, making it easy to match SWOT observations. For illustrative convenience, we focus on a pair of SWOT SSH (Figure S1a in Supporting Information S1) and HFR SSV (Figures S1b–S1c in Supporting Information S1) at ~2023-09-11 17:30:00. Figures S1d–S1f in Supporting Information S1 show SSH and SSV which are remapped onto SWOT swaths.

Prior to the application of the PV-based method to the real-ocean observations, we employ modeled SSH and SSV from the MITgcm LLC4320 simulation as a testbed. This global simulation has a horizontal grid spacing of

~2 km and outputs hourly snapshot variables from September 2011 to November 2012. In this study, we use the hourly model output offshore of California during September 2012. Figures S2a–S2c in Supporting Information S1 display the simulated SSH and SSV at 2012-09-11 17:30:00; SSH and SSV at the same time, which are remapped onto SWOT swaths, are shown in Figures S2d–S2f in Supporting Information S1. More details about the LLC4320 simulation can be found in Arbic et al. (2018).

2.2. The PV-Based Separation

In the following, we concisely describe the mathematical formulations of the PV-based method for a rotating shallow water system; for further details, we refer to Zeitlin (2018) and C. Wang et al. (2025). That is,

$$\nabla^2\left(\frac{g\overline{\eta}}{f_0}\right)-\frac{1}{L_d^2}\frac{g\overline{\eta}}{f_0}=\zeta-\frac{1}{L_d^2}\frac{g\eta}{f_0} \tag{1}$$

$$\boldsymbol{f_0}\times\overline{\boldsymbol{u}}=-g\nabla\overline{\eta} \tag{2}$$

$$\eta'=\eta-\overline{\eta} \tag{3}$$

$$\boldsymbol{u}'=\boldsymbol{u}-\overline{\boldsymbol{u}} \tag{4}$$

where the overbar represents the vortical variable, the prime the wavy variable, $\boldsymbol{u}=(u,v)$ SSV, η SSH, $\zeta=\frac{\partial v}{\partial x}-\frac{\partial u}{\partial y}$ the vertical component of the relative vorticity (hereafter referred simply to as the relative vorticity), g the acceleration due to gravity, $\boldsymbol{f_0}=\left(0,0,f_0\right)$ with f_0 being the Coriolis parameter and L_d the deformation radius. It is emphasized that we adopt a pragmatic manner to define L_d as the effective deformation radius (Figure S3 in Supporting Information S1) which considers contributions of all vertical modes; detailed introductions to the determination of L_d can be found in Section S1 of Supporting Information S1. Due to the peculiar domain geometry of SWOT data, the procedures for solving Equations 1–4 in the present study are quite different from those in C. Wang et al. (2025); see Section S1 in Supporting Information S1 for details. We also use the decomposition approach of C. Wang et al. (2023a) to obtain baseline vortical and wavy variables for the LLC4320 simulation and validate the PV-based separation results against those baseline truth; more information about the baseline separation is given in Section S2 in Supporting Information S1 where Lagrangian filtering (Shakespeare et al., 2021) is additionally introduced to demonstrate that the decomposition approach of C. Wang et al. (2023a) well serves as the baseline.

3. Results

3.1. Decomposed Variables Using the Numerical Model Data

In this section, we apply the PV-based method to the LLC4320 simulation. The separated wavy SSH, zonal velocity and meridional velocity are shown in Figures 1a–1c, respectively. Due to the strong incoherence of baroclinic tides offshore of California (Kachelein et al., 2024), wavy SSH and SSV are dominated by irregular spatial patterns. Those irregular features essentially follow the dispersion relation curves of internal gravity waves and tidal frequencies in the frequency-wavenumber spectra (Figures S4a and S4d in Supporting Information S1) which are calculated after the PV-based method is applied to each snapshot of SSH and SSV. Compared with wavy SSH and SSV, the irregular patterns in wavy horizontal divergence (Figure 2a) and wavy relative vorticity (Figure 2b) are characterized by much finer horizontal scales since the spatial differentiation tends to amplify the contributions from high-wavenumber features (C. Wang et al., 2023b). Constrained by the relative vorticity equation in spectral space (i.e., Equation 5 below) of internal gravity waves whose frequency is larger than f_0, the magnitude of wavy horizontal divergence (solid red line in Figure 3) is generally larger than that of wavy relative vorticity (solid blue line) and such magnitude difference generally becomes more pronounced with the increasing wavenumber.

$$i\omega\widehat{\zeta'}+f_0\widehat{\chi'}=0 \tag{5}$$

10.1029/2024GL113995

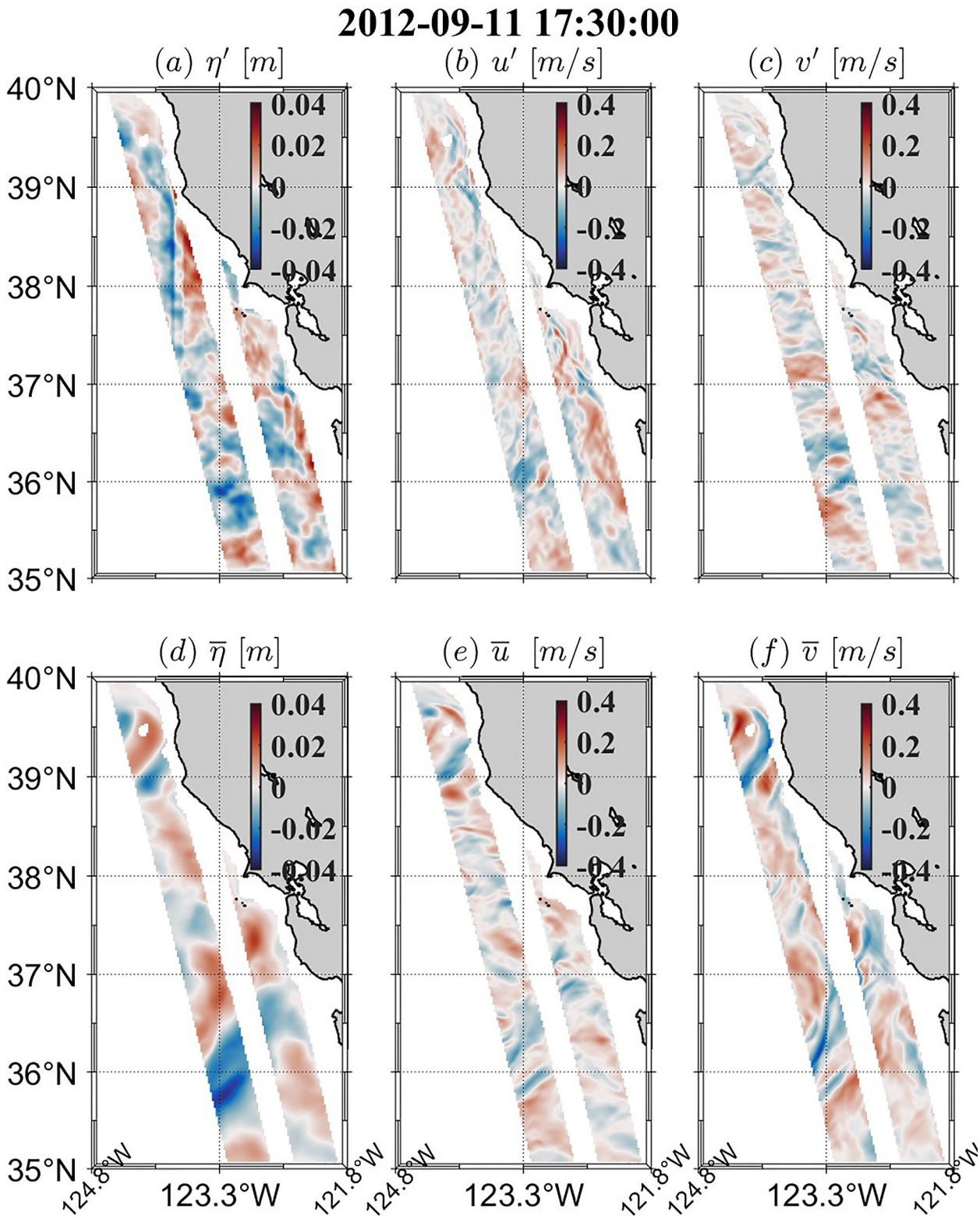

Figure 1. The decomposed sea surface height (a, d), zonal velocity (b, e) and meridional velocity (c, f) based on the LLC4320 simulation offshore of California. The upper (a–c) and lower (d–f) panels represent wavy and vortical motions, respectively.

10.1029/2024GL113995

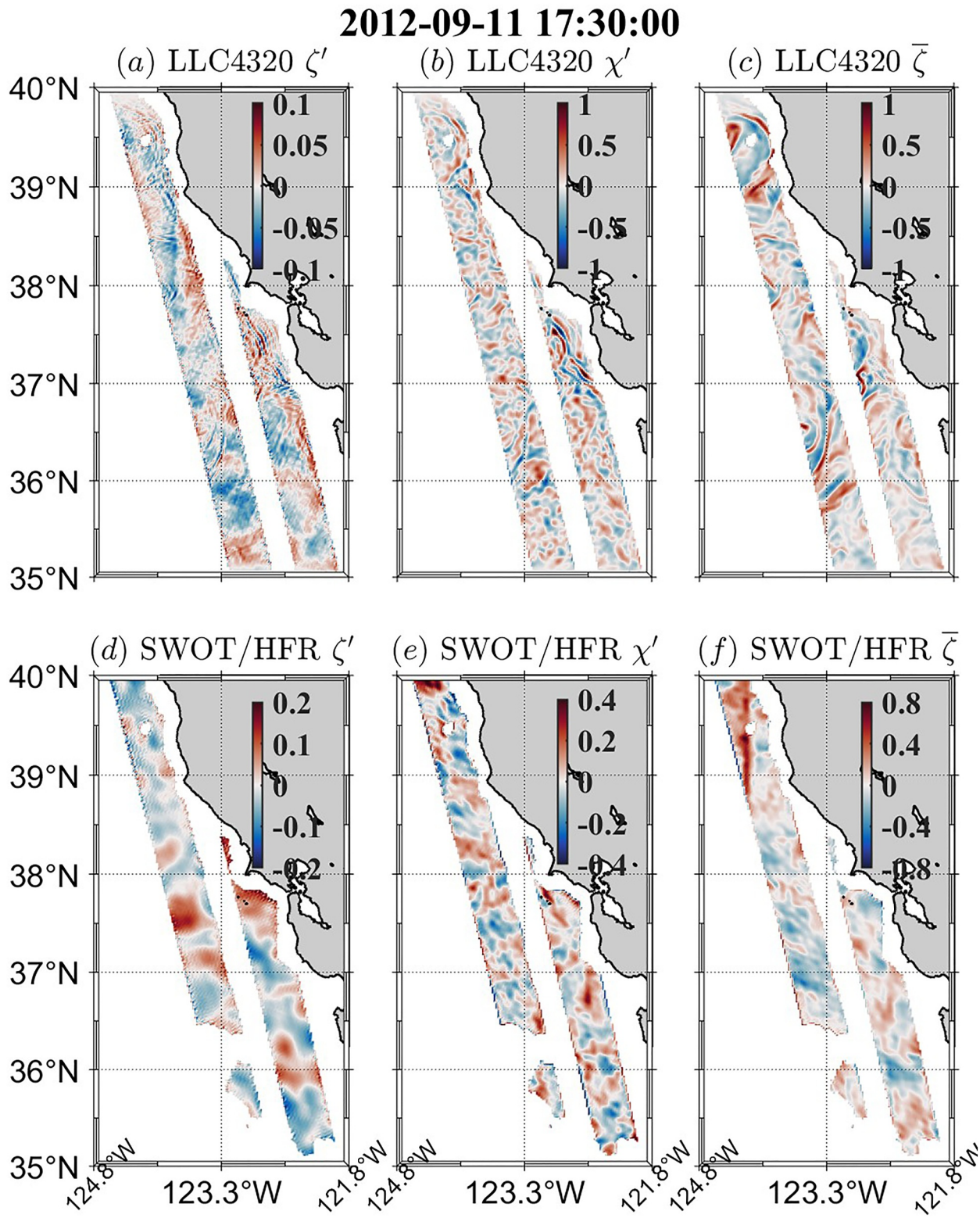

Figure 2. The decomposed relative vorticity (a, c, d, f) and horizontal divergence (b, e) based on LLC4320 (a–c) and Surface Water and Ocean Topography (SWOT)/high-frequency radar (HFR) (d–f) offshore of California. The first two columns (a, b, d, e) and third (c, f) column represent wavy and vortical motions, respectively. Note the different color scales between LLC4320 and SWOT/HFR.

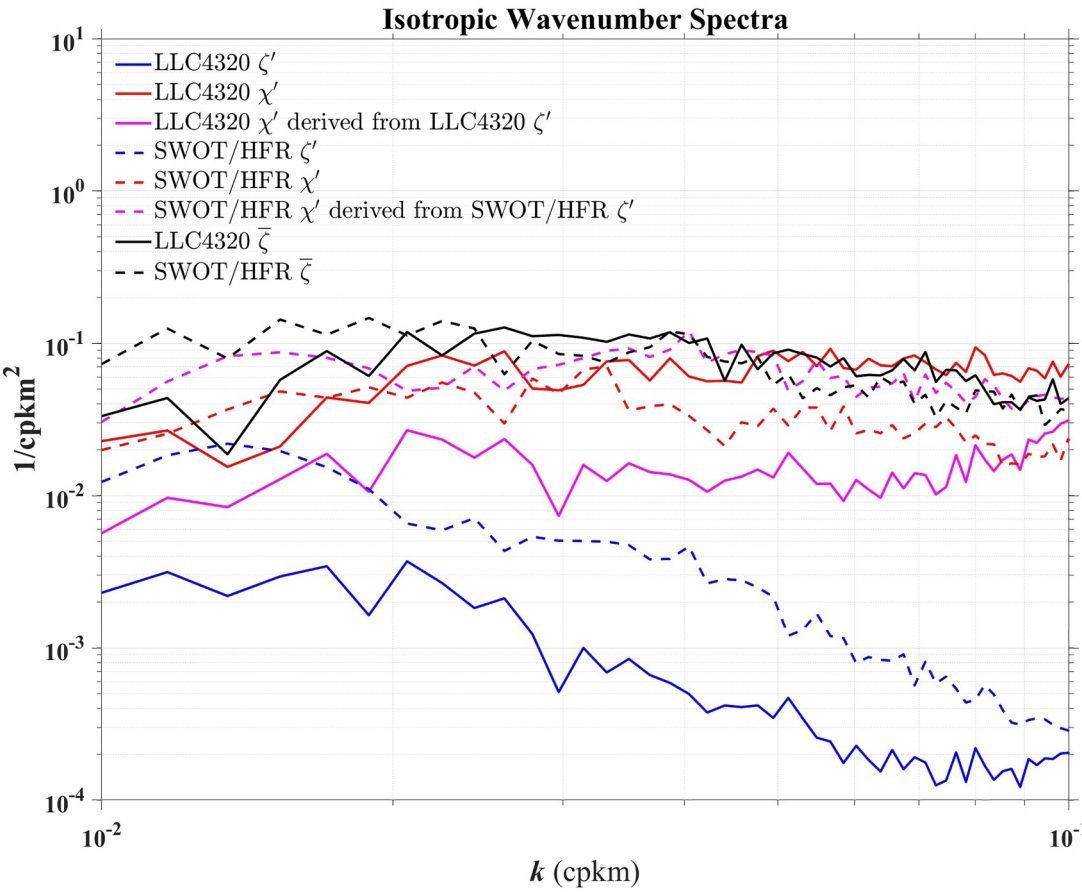

Figure 3. The isotropic wavenumber spectra for wavy and vortical motions. The solid and dashed lines are based on LLC4320 and Surface Water and Ocean Topography/high-frequency radar, respectively. The blue, red and black lines show wavy relative vorticity, wavy horizontal divergence and vortical relative vorticity, respectively. The magenta lines represent wavy horizontal divergence derived from wavy relative vorticity. Note that the plot is cut at 10^{-2} and 10^{-1} cpkm to remove the artificial effect of zero-filling.

where the caret (^) denotes Fourier-transformed variables, χ is the horizontal divergence and $\omega^2 = c_e^2 K^2 + f_0^2$ with K representing the isotropic wavenumber and c_e the phase speed corresponding to L_d defined in Section S1 of Supporting Information S1. Using Equation 5, we can derive wavy horizontal divergence from wavy relative vorticity; it is found that although there exists a magnitude difference between the target (solid red line in Figure 3) and derived (solid magenta line) divergence wavenumber spectra, variations of the spectra with the increasing wavenumber seem to be quite consistent. This tends to suggest the dynamical consistency among wavy vorticity and divergence. The consistency is re-confirmed by the joint probability distribution function patterns of $\zeta' - \chi'$ in Figure S5a in Supporting Information S1 and $\zeta' - \sigma'$ (σ is the strain) in Figure S5b in Supporting Information S1 (Xiao et al., 2023). To further quantitatively assess how well the PV-based method works, we validate the separated wavy variables against the baseline truth. For wavy SSH (SSV), the root mean square errors (Figures S6a–S6c in Supporting Information S1) between the PV-based and baseline results are generally smaller than 0.008 m (0.06 m/s) over the entire domain and negligible compared with its typical magnitude (i.e., 0.04 for wavy SSH and 0.4 for wavy SSV in Figure 1a–1c); the correlation coefficients (Figures S7a–S7c in Supporting Information S1) are above 0.8 over almost the whole study region. The small root mean square errors and high correlations suggest that wavy motions derived from the PV-based method agree well with the baseline in terms of the magnitude, spatial pattern and temporal evolution.

The vortical SSH, zonal velocity and meridional velocity are displayed in Figure 1d–1f, respectively. Both mesoscale and submesoscale features are revealed. Submesoscale vorticity filaments are particularly clear in Figure 2c. The joint probability distribution function pattern of $\overline{\zeta} - \overline{\sigma}$ in Figure S5c in Supporting Information S1 is representative of vortical motions (Rocha et al., 2016; Shcherbina et al., 2013; Xiao et al., 2023). The horizontal

divergence vanishes (not shown) since vortical SSH and SSV are in geostrophic balance by construction. The wavenumber-frequency spectra in Figures S4b–S4e in Supporting Information S1 show that vortical motions are mostly sub-inertial. Although there exists some spectral energy leakage at the tidal and near-inertial frequencies, the extraction of vortical motions is at least satisfactory (Figures S4c–S4f in Supporting Information S1). The quantitative comparision with the baseline vortical variables, in terms of small root mean square errors in Figures S6d–S6f in Supporting Information S1 and high correlation in Figures S7d–S7f in Supporting Information S1, demonstrates a favorable agreement.

Overall, the PV-based method proves satisfactorily applicable to pseudo-SWOT data based on the LLC4320 simulation. In the next section, we apply this separation method to the real-ocean observational data.

3.2. Decomposed Variables Using SWOT/HFR Measurements

Figure 4 shows vortical and wavy SSH and SSV separated from SWOT/HFR measurements. The corresponding horizontal divergence and relative vorticity are shown in Figure 2d–2f. The irregular spatial distributions of wavy variables (Figures 2d and 2e and 4a–4c) indicate the dominant contribution of incoherent baroclinic tides offshore of California, which has been recently confirmed by HFR data (Kachelein et al., 2024). As explained in Section 3.1, the wave dynamics requires that wavy relative vorticity (Figure 2d) is dominated by a larger horizontal scale but a smaller magnitude than wavy horizontal divergence (Figure 2e); again, this magnitude distinction becomes clearer as the wavenumber increases, as shown by the dashed blue and red lines in Figure 3. The spectra of the derived wavy horizontal divergence (dashed magenta line in Figure 3) expectedly follow that of the target one (dashed red line). It is interesting to note that compared with SWOT/HFR, the LLC4320 simulation well reproduces the spectral energy level of wavy horizontal divergence but underestimates that of wavy relative vorticity. These results appear to agree with the previous finding that LLC4320 lies close to McLane profiling observations in the supertidal band (Savage et al., 2017) which is more dominated by horizontal divergence than relative vorticity. For vortical variables (Figures 2f and 4d–4f), abundant mesoscale features in geostrophic balance and without horizontal divergence are revealed. The submesoscale processes with high relative vorticity are also identifiable, especially in Figure 2f. However, filamentary structures present in LLC4320 (i.e., Figure 2c) are lacking in SWOT/HFR (i.e., Figure 2f); there are many potential reasons but one could be the spatial resolution contrast (i.e., 6 vs. 2 km) between the HFR and LLC4320 data. Otherwise, LLC4320 and SWOT/HFR vortical relative vorticity fields have the same energy across all scales as shown by solid and dashed black lines in Figure 3; this highlights the usefulness of the high-resolution simulation in interpreting SWOT/HFR data. Comparatively, vortical and wavy variables in this oceanic region have the same magnitude. As a result, wavy SSH could distort or overwhelm vortical SSH, re-emphasizing the importance of removing the wavy signal prior to utilizing SWOT SSH for (sub)mesoscale-related studies. Therefore, it is informative to compare the vortical SSH extracted from SWOT data with the nadir-looking altimetric SSH (i.e., AVISO SSH). For comparison, we use the nearest-neighbor interpolation to remap AVISO SSH onto the finer grid of SWOT vortical SSH since this interpolation method does not introduce artificial submesoscale features. It is found that after the removal of the wavy signal, the general pattern of SWOT vortical SSH (Figure 4d or Figure S8a in Supporting Information S1) qualitatively agrees with that of AVISO SSH (Figure S8b in Supporting Information S1). However, their quantitative difference reaches a non-negligible magnitude of ∼0.04 m (Figure S8c in Supporting Information S1); importantly, the difference contains both mesoscale (i.e., pixel scale in Figure S8c in Supporting Information S1) and submesoscale (i.e., sub-pixel scale in Figure S8c in Supporting Information S1) features. This indicates that the SWOT satellite not only improves the accuracy of observing mesoscale eddies but also achieves the intention of capturing submesocale currents.

4. Summary and Discussion

Realizing the concurrent availability of HFR SSV and SWOT SSH, we use a PV-based method to address the challenge of separating vortical and wavy motions intermingled in those observations. This PV-based separation is exactly the linear normal mode initialization which has played an important role in the history of numerical weather prediction. When applied to concurrent SSH and SSV extracted from the LLC4320 simulation and remapped onto SWOT swaths offshore of California, the PV-based method shows good performance compared with the baseline truth. The performance supports the utility of this method to swath-style data and motivates its application to real-ocean observations. With SSH and SSV respectively from the SWOT satellite and the HFR system offshore of California, the separated results confirm the capability of the SWOT satellite to capture

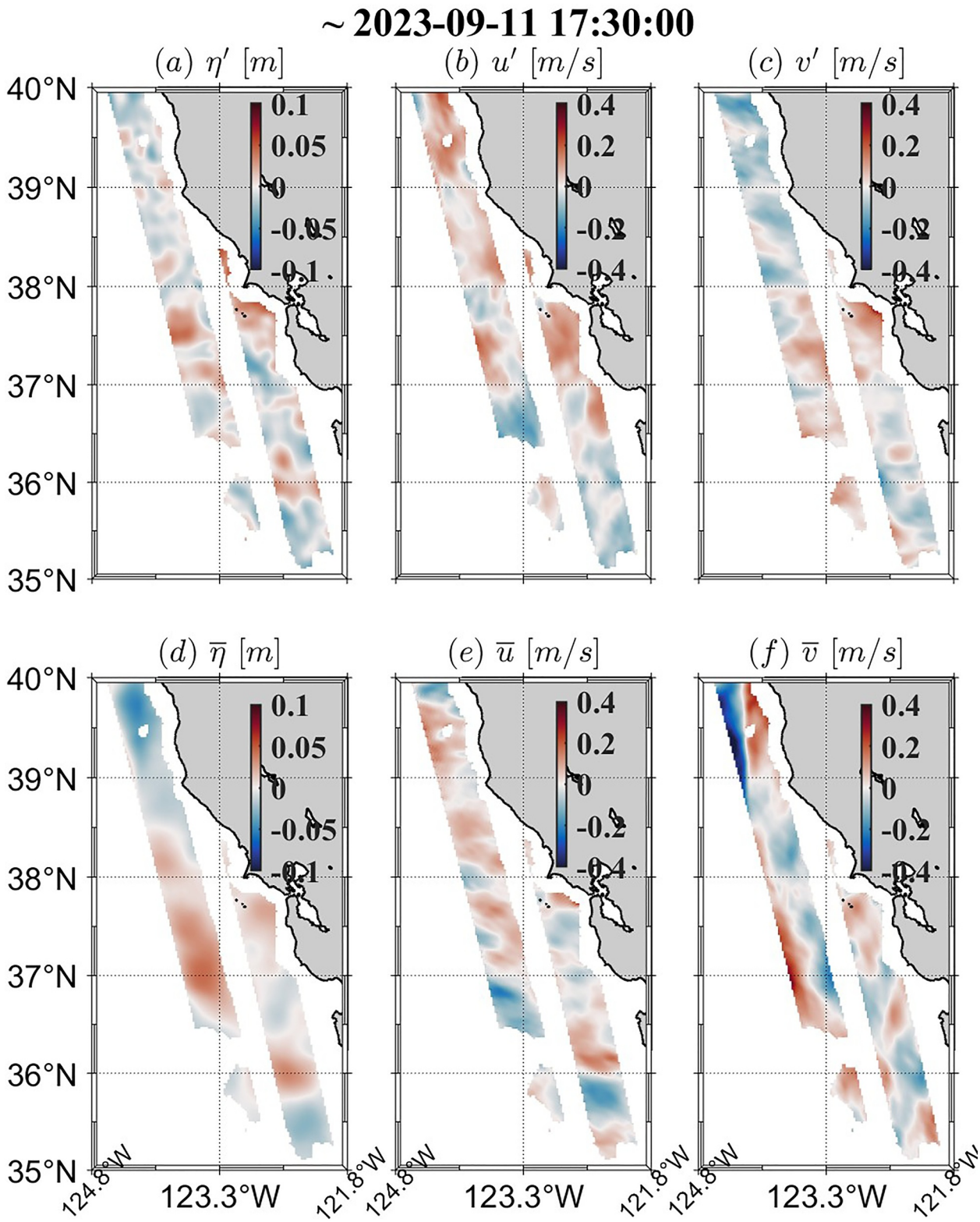

Figure 4. Same as Figure 1 but based on Surface Water and Ocean Topography/high-frequency radar measurements.

submesoscale processes, highlight the necessity of removing the wavy signal before conducting (sub)mesoscale-oriented studies and reveal the general pattern agreement between vortical SSH observed by SWOT and SSH by the conventional satellite altimeter.

Since separating vortical and wavy motions in SWOT measurements is a challenging difficulty, we regard this study as a first-step attempt towards a more accurate separation; therefore, it is necessary to clearly discuss the limitations of the present study and potential improvements in future studies.

Firstly, the present study particularly applies to the regime where (a) Rossby and Froude numbers are small and (b) vortical and wavy motions have comparable magnitude. Beyond that parameter regime, the theoretical basis of this study that wavy motions carry no PV anomaly breaks down. For example, the stronger internal gravity waves can non-negligibly modulate the PV anomaly of the weaker vortical motions (Bühler & McIntyre, 1998; Rocha et al., 2018; Wagner & Young, 2015; Xie & Vanneste, 2015). The gravity-wave-induced forcing can even resonantly trigger Rossby waves (Bühler & McIntyre, 1998). More complicated initialization techniques, such as nonlinear normal mode initialization (Baer & Tribbia, 1977; Chouksey et al., 2018; Machenhauer, 1977), digital filtering (Lynch et al., 1997; Lynch & Huang, 1992), quasi-geostrophic theory with a next-order correction (Dù & Smith, 2024; Spall & McWilliams, 1992; Vallis, 1996; Warn et al., 1995), optimal PV balance (Viúdez & Dritschel, 2004) and optimal balance (Chouksey et al., 2023; Masur & Oliver, 2020; Rosenau et al., 2025), have the potential to consider most/all parameter regimes and merit a future pursuit.

Secondly, that the PV anomaly is zero is a necessary rather than sufficient condition for wavy motions. Typical examples of PV-free vortical motions include the surface quasi-geostrophic current in particular (Held et al., 1995; Guillaume Lapeyre, 2017) and the Eady-like flow in general (e.g., Callies et al., 2015; Molemaker et al., 2010). As can be seen in Section 2.2, Equation 1 is exactly the interior quasi-geostrophic theory; consequently, vortical motions driven by the surface and/or bottom buoyancy anomaly might be misclassified into the wavy category. However, this misclassification might not pose a serious problem in the present study region with low mesoscale kinetic energies since buoyancy-driven vortical motions are most active in oceanic regions with intense mesoscale activities (Gonzalez-Haro & Isern-Fontanet, 2012, 2014). To consider the boundary buoyancy effects and thus improve the vortical-wavy separation, it is necessary to additionally invoke the surface quasi-geostrophic theory which involves a third variable, namely sea surface density.

Thirdly, the main drawback of the PV-based method might be to assume that all vortical motions are in geostrophic balance and thus do not have horizontal divergence. This assumption can be problematic for submesoscale currents (Archer et al., 2025; Tranchant et al., 2025) and even for ∼100-km rings (Penven et al., 2014). The abovementioned advanced initialization techniques, which do not a priori assume the geostrophic balance, are capable of addressing this drawback.

Fourthly, given that our main goal is to test the usefulness of the PV-based method, we assume a rotating shallow water system with an effective deformation radius to simplify the challenging vortical-wavy separation. Combined with well-established subsurface reconstruction methods for (sub)mesoscale processes (Klein et al., 2009; LaCasce & Mahadevan, 2006; Lapeyre & Klein, 2006; Liu et al., 2019; Qiu et al., 2016; J. Wang et al., 2013) and internal gravity waves (Ray & Cartwright, 2001; Zhao, 2017; Zhao et al., 2016), the present study easily extends to the continuously stratified system.

Fifthly, we use the decomposition approach of C. Wang et al. (2023a) as the baseline. As mentioned in C. Wang et al. (2023a), this approach has some limitations. For example, the Gibbs phenomenon occurs due to the spectral cutoff characteristic of the 0/1-type filter; that vortical and wavy motions are mutually exclusive in spectral space is assumed. How these limitations affect the validation of the vortical-wavy separation in the present study remains unknown. We plan to pursue this in the future.

Finally, HFR data usually suffer from observational errors (Clary et al., 2019) whose adverse effects on the physical processes of interest remain to be explored in detail. In future studies, a realistic tide-resolving and submesoscale-admitting simulation simultaneous with SWOT and HFR observations could be made in order to quantify to what extent measurement limitations or inaccuracies contaminate the vortical-wavy separation.

Overall, this study suggests a promising research direction involving SWOT/HFR measurements. At the present time, the HFR system provides SSV observations over the coastal ocean; in the future, the Doppler scatterometric satellite will measure a wide swath of SSV over the global ocean (Du et al., 2021; H. Torres et al., 2023).

Hopefully, this study would help understand multiscale ocean dynamics invigorated by those wide-swath satellite missions.

Data Availability Statement

The SWOT Level-3 SSH Expert product is available at https://doi.org/10.24400/527896/A01-2023.018 (AVISO/DUACS, 2024). The high-frequency radar SSV data can be downloaded at https://doi.org/10.48670/moi-00041 (E.U. Copernicus Marine Service Information, 2024a). The nadir-looking satellite altimeter data are available from https://doi.org/10.48670/moi-00148 (E.U. Copernicus Marine Service Information, 2024b). The model output of the LLC4320 simulation can be accessed from https://data.nas.nasa.gov/ecco/data.php?dir=/eccodata/llc_4320 (ECCO Consortium, 2025). The PV-based separation code adapted for SWOT and HFR data is accessible at https://doi.org/10.5281/zenodo.14088311 (C. Wang, 2024).

Acknowledgments
This work was supported by the Southern Marine Science and Engineering Guangdong Laboratory (Zhuhai) (SML2022SP401, 2023SP207), the National Natural Science Foundation of China (92258301, 42406021, and 42076013), the Natural Science Foundation of Fujian Province of China (2021J02005 and 2021J01024), and the National Key R&D Program of China (2023YFE0126700). We are indebted to two anonymous reviewers whose constructive comments and suggestions have greatly improved this study.

References

Arbic, B. K., Alford, M. H., Ansong, J. K., Buijsman, M. C., Ciotti, R. B., Farrar, J. T., et al. (2018). A primer on global internal tide and internal gravity wave continuum modeling in HYCOM and MITgcm. *New Frontiers in Operational Oceanography*, 307–392. https://doi.org/10.17125/gov2018.ch13

Archer, M., Wang, J., Klein, P., Dibarboure, G., & Fu, L. (2025). Wide-swath satellite altimetry unveils global submesoscale ocean dynamics. *Nature*, *640*(8059), 691–696. https://doi.org/10.1038/s41586-025-08722-8

AVISO/DUACS. (2024). SWOT level-3 KaRIn low rate SSH expert (v0.3) [Dataset]. *CNES*. https://doi.org/10.24400/527896/A01-2023.018

Baer, F., & Tribbia, J. J. (1977). On complete filtering of gravity modes through nonlinear initialization. *Monthly Weather Review*, *105*(12), 1536–1539. https://doi.org/10.1175/1520-0493(1977)105<1536:ocfogm>2.0.co;2

Bühler, O., & McIntyre, M. E. (1998). On non-dissipative wave-mean interactions in the atmosphere or oceans. *Journal of Fluid Mechanics*, *354*, 301–343. https://doi.org/10.1017/S002211209700774X

Callies, J., Flierl, G., Ferrari, R., & Fox-Kemper, B. (2015). The role of mixed-layer instabilities in submesoscale turbulence. *Journal of Fluid Mechanics*, *788*, 5–41. https://doi.org/10.1017/jfm.2015.700

Carrère, L., Le Provost, C., & Lyard, F. (2004). On the statistical stability of the M_2 barotropic and baroclinic tidal characteristics from along-track TOPEX/Poseidon satellite altimetry analysis. *Journal of Geophysical Research*, *109*(3), 1–13. https://doi.org/10.1029/2003jc001873

Chavanne, C., Flament, P., & Gurgel, K. W. (2010). Interactions between a submesoscale anticyclonic vortex and a front. *Journal of Physical Oceanography*, *40*(8), 1802–1818. https://doi.org/10.1175/2010JPO4055.1

Chouksey, M., Eden, C., & Brüggemann, N. (2018). Internal gravity wave emission in different dynamical regimes. *Journal of Physical Oceanography*, *48*(8), 1709–1730. https://doi.org/10.1175/JPO-D-17-0158.1

Chouksey, M., Eden, C., Masur, G. T., & Oliver, M. (2023). A comparison of methods to balance geophysical flows. *Journal of Fluid Mechanics*, *971*, 1–19. https://doi.org/10.1017/jfm.2023.602

Clary, J., Nadeau, L. P., & Chavanne, C. (2019). The effect of measurement limitations on high-frequency radar-derived spectral energy fluxes. *Journal of Atmospheric and Oceanic Technology*, *36*(11), 2139–2152. https://doi.org/10.1175/JTECH-D-18-0237.1

Coiffier, J. (2011). *Fundamentals of numerical weather prediction*. Cambridge University Press.

Dickinson, R. E., & Williamson, D. L. (1972). Free oscillations of a discrete stratified fluid with application to numerical weather prediction. *Journal of the Atmospheric Sciences*, *29*(4), 623–640. https://doi.org/10.1175/1520-0469(1972)029<0623:FOOADS>2.0.CO;2

Dù, R. S., & Smith, K. S. (2024). Emergent vorticity asymmetry of one and two-layer shallow water system captured by a next-order balanced model. Retrieved from http://arxiv.org/abs/2411.02291

Du, Y., Dong, X., Jiang, X., Zhang, Y., Zhu, D., Sun, Q., et al. (2021). Ocean surface current multiscale observation mission (OSCOM): Simultaneous measurement of ocean surface current, vector wind, and temperature. *Progress in Oceanography*, *193*, 102531. https://doi.org/10.1016/j.pocean.2021.102531

Dushaw, B. D. (2015). An empirical model for mode-1 internal tides derived from satellite altimetry: Computing accurate tidal predictions at arbitrary points over the world oceans. Retrieved from http://www.apl.washington.edu/project/%0Aprojects/tm_1-15/pdfs/tm_1_15.pdf

ECCO Consortium. (2025). LLC4320 [Dataset]. *ECCO*. Retrieved from https://data.nas.nasa.gov/ecco/data.php?dir=/eccodata/llc_4320

E.U. Copernicus Marine Service Information. (2024a). Global ocean gridded L4 sea surface heights and derived variables reprocessed 1993 ongoing [Dataset]. *Stl*. https://doi.org/10.48670/moi-00148

E.U. Copernicus Marine Service Information. (2024b). Global ocean-in-situ near real time observations of ocean currents [Dataset]. *Stl*. https://doi.org/10.48670/moi-00041

Fu, L. L., Pavelsky, T., Cretaux, J. F., Morrow, R., Farrar, J. T., Vaze, P., et al. (2024). The Surface Water and Ocean Topography mission: A breakthrough in radar remote sensing of the ocean and land surface water. *Geophysical Research Letters*, *51*(4), 1–9. https://doi.org/10.1029/2023GL107652

Gao, Z., Chapron, B., Ma, C., Fablet, R., Febvre, Q., Zhao, W., & Chen, G. (2024). A deep learning approach to extract balanced motions from sea surface height snapshot. *Geophysical Research Letters*, *51*(7). https://doi.org/10.1029/2023GL106623

Gonzalez-Haro, C., & Isern-Fontanet, J. (2012). Ocean surface currents reconstruction at a global scale from microwave measurements. *International Geoscience and Remote Sensing Symposium (IGARSS)*, 3780–3783. https://doi.org/10.1109/IGARSS.2012.6350494

González-Haro, C., & Isern-Fontanet, J. (2014). Global ocean current reconstruction from altimetric and microwave SST measurements. *Journal of Geophysical Research: Oceans*, *119*(6), 3378–3391. https://doi.org/10.1002/2013JC009728

Hart-Davis, M. G., Andersen, O. B., Ray, R. D., Zaron, E. D., Schwatke, C., Arildsen, R. L., et al. (2024). Tides in complex coastal regions: Early case studies from wide-swath SWOT measurements. *Geophysical Research Letters*, *51*(20). https://doi.org/10.1029/2024GL109983

Held, I. M., Pierrehumbert, R. T., Garner, S. T., & Swanson, K. L. (1995). Surface quasi-geostrophic dynamics. *Journal of Fluid Mechanics*, *282*, 1–20. https://doi.org/10.1017/S0022112095000012

Kachelein, L., Gille, S. T., Mazloff, M. R., & Cornuelle, B. D. (2024). Characterizing non-phase-locked tidal currents in the California Current System using high-frequency radar. *Journal of Geophysical Research: Oceans*, *129*(7). https://doi.org/10.1029/2023JC020340

Kantha, L. H., & Tierney, C. C. (1997). Global baroclinic tides. *Progress in Oceanography*, *40*(1–4), 163–178. https://doi.org/10.1016/S0079-6611(97)00028-1

Klein, P., Isem-Fontanet, J., Lapeyre, G., Roullet, G., Danioux, E., Chapron, B., et al. (2009). Diagnosis of vertical velocities in the upper ocean from high resolution sea surface height. *Geophysical Research Letters*, *36*(12), 1–5. https://doi.org/10.1029/2009GL038359

Klein, P., Lapeyre, G., Siegelman, L., Qiu, B., Fu, L., Torres, H., et al. (2019). Ocean-scale interactions from space. *Earth and Space Science*, *6*(5), 795–817. https://doi.org/10.1029/2018EA000492

LaCasce, J. H., & Mahadevan, A. (2006). Estimating subsurface horizontal and vertical velocities from sea-surface temperature. *Journal of Marine Research*, *64*(5), 695–721. https://doi.org/10.1357/002224006779367267

Lai, Y., Zhou, H., Yang, J., Zeng, Y., & Wen, B. (2017). Submesoscale eddies in the Taiwan Strait observed by high-frequency radars: Detection algorithms and eddy properties. *Journal of Atmospheric and Oceanic Technology*, *34*(4), 939–953. https://doi.org/10.1175/JTECH-D-16-0160.1

Lapeyre, G. (2017). Surface quasi-geostrophy. *Fluids*, *2*(1), 7. https://doi.org/10.3390/fluids2010007

Lapeyre, G., & Klein, P. (2006). Dynamics of the upper oceanic layers in terms of surface quasigeostrophy theory. *Journal of Physical Oceanography*, *36*(2), 165–176. https://doi.org/10.1175/JPO2840.1

Le Guillou, F., Lahaye, N., Ubelmann, C., Metref, S., Cosme, E., Ponte, A., et al. (2021). Joint estimation of balanced motions and internal tides from future wide-swath altimetry. *Journal of Advances in Modeling Earth Systems*, *13*(12), 1–17. https://doi.org/10.1029/2021MS002613

Lee, E. A., & Kim, S. Y. (2022). An investigation of the Helmholtz and wave-vortex decompositions on surface currents in a coastal region. *Continental Shelf Research*, *238*, 104683. https://doi.org/10.1016/j.csr.2022.104683

Lguensat, R., Fablet, R., Le Sommer, J., Metref, S., Cosme, E., Ouenniche, K., et al. (2020). Filtering internal tides from wide-swath altimeter data using convolutional neural networks. *International Geoscience and Remote Sensing Symposium (IGARSS)*, 3904–3907. https://doi.org/10.1109/IGARSS39084.2020.9323531

Liu, L., Xue, H., & Sasaki, H. (2019). Reconstructing the ocean interior from high-resolution sea surface information. *Journal of Physical Oceanography*, *49*(12), 3245–3262. https://doi.org/10.1175/JPO-D-19-0118.1

Lynch, P., Giard, D., & Ivanovici, V. (1997). Improving the efficiency of a digital filtering scheme for diabatic initialization. *Monthly Weather Review*, *125*(8), 1976–1982. https://doi.org/10.1175/1520-0493(1997)125<1976:ITEOAD>2.0.CO;2

Lynch, P., & Huang, X.-Y. (1992). Initialization of the HIRLAM model using a digital filter. *Monthly Weather Review*, *120*(6), 1019–1034. https://doi.org/10.1175/1520-0493(1992)120<1019:IOTHMU>2.0.CO;2

Machenhauer, B. (1977). On the dynamics of gravity oscillations in a shallow water model, with application to normal mode initialization. *Contributions to the Physics of the Atmosphere*, *50*, 253–271.

Masur, G. T., & Oliver, M. (2020). Optimal balance for rotating shallow water in primitive variables. *Geophysical & Astrophysical Fluid Dynamics*, *114*(4–5), 429–452. https://doi.org/10.1080/03091929.2020.1745789

Molemaker, M. J., McWilliams, J. C., & Capet, X. (2010). Balanced and unbalanced routes to dissipation in an equilibrated Eady flow. *Journal of Fluid Mechanics*, *654*, 35–63. https://doi.org/10.1017/S0022112009993272

Morrow, R., Fu, L.-L., Rio, M.-H., Ray, R., Prandi, P., Le Traon, P.-Y., & Benveniste, J. (2023). Ocean circulation from space. *Surveys in Geophysics*, *44*(5), 1243–1286. https://doi.org/10.1007/s10712-023-09778-9

Morrow, R., Fu, L. L., Ardhuin, F., Benkiran, M., Chapron, B., Cosme, E., et al. (2019). Global observations of fine-scale ocean surface topography with the Surface Water and Ocean Topography (SWOT) mission. *Frontiers in Marine Science*, *6*, 1–19. https://doi.org/10.3389/fmars.2019.00232

Payandeh, A. R., Washburn, L., Emery, B., & Ohlmann, J. C. (2023). The occurrence, variability, and potential drivers of submesoscale eddies in the Southern California Bight based on a decade of high-frequency radar observations. *Journal of Geophysical Research: Oceans*, *128*(10), 1–20. https://doi.org/10.1029/2023JC019914

Pedlosky, J. (2003). *Waves in the ocean and atmosphere*. Springer Berlin Heidelberg. https://doi.org/10.1007/978-3-662-05131-3

Penven, P., Halo, I., Pous, S., & Marié, L. (2014). Cyclogeostrophic balance in the Mozambique channel. *Journal of Geophysical Research: Oceans*, *119*(2), 1054–1067. https://doi.org/10.1002/2013JC009528

Qiu, B., Chen, S., Klein, P., Ubelmann, C., Fu, L. L., & Sasaki, H. (2016). Reconstructability of three-dimensional upper-ocean circulation from SWOT sea surface height measurements. *Journal of Physical Oceanography*, *46*(3), 947–963. https://doi.org/10.1175/JPO-D-15-0188.1

Qiu, B., Chen, S., Wang, J., & Fu, L. L. (2024). Seasonal and fortnight variations in internal solitary saves in the Indonesian Seas from the SWOT measurements. *Journal of Geophysical Research: Oceans*, *129*(7), 1–11. https://doi.org/10.1029/2024JC021086

Ray, R. D., & Cartwright, D. E. (2001). Estimates of internal tide energy fluxes from Topex/Poseidon altimetry: Central North Pacific. *Geophysical Research Letters*, *28*(7), 1259–1262. https://doi.org/10.1029/2000GL012447

Ray, R. D., & Mitchum, G. T. (1996). Surface manifestation of internal tides generated near Hawaii. *Geophysical Research Letters*, *23*(16), 2101–2104. https://doi.org/10.1029/96GL02050

Ray, R. D., & Zaron, E. D. (2016). M_2 internal tides and their observed wavenumber spectra from satellite altimetry. *Journal of Physical Oceanography*, *46*(1), 3–22. https://doi.org/10.1175/JPO-D-15-0065.1

Rocha, C. B., Gille, S. T., Chereskin, T. K., & Menemenlis, D. (2016). Seasonality of submesoscale dynamics in the Kuroshio extension. *Geophysical Research Letters*, *43*(21), 304–311. https://doi.org/10.1002/2016GL071349

Rocha, C. B., Wagner, G. L., & Young, W. R. (2018). Stimulated generation: Extraction of energy from balanced flow by near-inertial waves. *Journal of Fluid Mechanics*, *847*, 417–451. https://doi.org/10.1017/jfm.2018.308

Rosenau, S. G., Chouksey, M., & Eden, C. (2025). Towards realistic ocean flow decomposition using optimal balance with time-averaging. 1–24. Retrieved from http://arxiv.org/abs/2501.11464

Savage, A. C., Arbic, B. K., Alford, M. H., Ansong, J. K., Farrar, J. T., Menemenlis, D., et al. (2017). Spectral decomposition of internal gravity wave sea surface height in global models. *Journal of Geophysical Research: Oceans*, *122*(10), 7803–7821. https://doi.org/10.1002/2017JC013009

Shakespeare, C. J., Gibson, A. H., Hogg, A. M. C., Bachman, S. D., Keating, S. R., & Velzeboer, N. (2021). A new open source implementation of Lagrangian filtering: A method to identify internal waves in high-resolution simulations. *Journal of Advances in Modeling Earth Systems*, *13*(10). https://doi.org/10.1029/2021MS002616

Shcherbina, A. Y., D'Asaro, E. A., Lee, C. M., Klymak, J. M., Molemaker, M. J., & McWilliams, J. C. (2013). Statistics of vertical vorticity, divergence, and strain in a developed submesoscale turbulence field. *Geophysical Research Letters*, *40*(17), 4706–4711. https://doi.org/10.1002/grl.50919

Soh, H. S., & Kim, S. Y. (2018). Diagnostic characteristics of submesoscale coastal surface currents. *Journal of Geophysical Research: Oceans*, *123*(3), 1838–1859. https://doi.org/10.1002/2017JC013428

Spall, M. A., & McWilliams, J. C. (1992). Rotational and gravitational influences on the degree of balance in the shallow-water equations. *Geophysical and Astrophysical Fluid Dynamics*, *64*(1–4), 1–29. https://doi.org/10.1080/03091929208228083

Tchilibou, M., Carrere, L., Lyard, F., Ubelmann, C., Dibarboure, G., Zaron, E. D., & Arbic, B. K. (2024). Internal tides off the amazon shelf in the western tropical Atlantic: Analysis of SWOT Cal/Val mission data. https://doi.org/10.5194/egusphere-2024-1857

Torres, H., Wineteer, A., Klein, P., Lee, T., Wang, J., Rodriguez, E., et al. (2023). Anticipated capabilities of the ODYSEA wind and current mission concept to estimate wind work at the air–sea interface. *Remote Sensing*, *15*(13). https://doi.org/10.3390/rs15133337

Torres, H. S., Klein, P., Siegelman, L., Qiu, B., Chen, S., Ubelmann, C., et al. (2019). Diagnosing ocean-wave-turbulence interactions from space. *Geophysical Research Letters*, *46*(15), 8933–8942. https://doi.org/10.1029/2019GL083675

Tranchant, Y., Legresy, B., Foppert, A., Pena-Molino, B., & Phillips, H. E. (2025). SWOT reveals fine-scale balanced motions and dispersion properties in the Antarctic Circumpolar Current. https://doi.org/10.22541/essoar.173655552.25945463/v1

Vallis, G. K. (1996). Potential vorticity inversion and balanced equations of motion for rotating and stratified flows. *Quarterly Journal of the Royal Meteorological Society*, *122*(529), 291–322. https://doi.org/10.1002/qj.49712252912

Viúdez, Á., & Dritschel, D. G. (2004). Optimal potential vorticity balance of geophysical flows. *Journal of Fluid Mechanics*. https://doi.org/10.1017/S0022112004002058

Wagner, G. L., & Young, W. R. (2015). Available potential vorticity and wave-averaged quasi-geostrophic flow. *Journal of Fluid Mechanics*, *785*, 401–424. https://doi.org/10.1017/jfm.2015.626

Wang, C. (2024). Separating vortical and wavy motions of oceanic flows with concurrent SWOT and high-frequency radar measurements [Dataset]. *Zenodo*. https://doi.org/10.5281/zenodo.14088311

Wang, C., Liu, Z., & Lin, H. (2023a). A simple approach for disentangling vortical and wavy motions of oceanic flows. *Journal of Physical Oceanography*, *53*(5), 1237–1249. https://doi.org/10.1175/JPO-D-22-0148.1

Wang, C., Liu, Z., & Lin, H. (2023b). On dynamical decomposition of multiscale oceanic motions. *Journal of Advances in Modeling Earth Systems*, *15*(3). https://doi.org/10.1029/2022MS003556

Wang, C., Liu, Z., Lin, H., Rocha, C., Yang, Q., Chen, D., & Gong, J. (2025). Disentangling wavy and vortical motions in concurrent snapshots of the sea surface height and velocity. *Ocean Modelling*, *196*, 102556. https://doi.org/10.1016/j.ocemod.2025.102556

Wang, H., Grisouard, N., Salehipour, H., Nuz, A., Poon, M., & Ponte, A. L. (2022). A deep learning approach to extract internal tides scattered by geostrophic turbulence. *Geophysical Research Letters*, *49*(11), 1–9. https://doi.org/10.1029/2022GL099400

Wang, J., Flierl, G. R., Lacasce, J. H., Mcclean, J. L., & Mahadevan, A. (2013). Reconstructing the ocean's interior from surface data. *Journal of Physical Oceanography*, *43*(8), 1611–1626. https://doi.org/10.1175/JPO-D-12-0204.1

Warn, T., Bokhove, O., Shepherd, T. G., & Vallis, G. K. (1995). Rossby number expansions, slaving principles, and balance dynamics. *Quarterly Journal of the Royal Meteorological Society*, *121*(523), 723–739. https://doi.org/10.1002/qj.49712152313

Williamson, D. L. (1976). Normal mode initialization procedure applied to forecasts with the global shallow water equations. *Monthly Weather Review*, *104*(2), 195–206. https://doi.org/10.1175/1520-0493(1976)104<0195:NMIPAT>2.0.CO;2

Xiao, Q., Balwada, D., Jones, C. S., Herrero-González, M., Smith, K. S., & Abernathey, R. (2023). Reconstruction of surface kinematics from sea surface height using neural networks. *Journal of Advances in Modeling Earth Systems*, *15*(10), 1–23. https://doi.org/10.1029/2023MS003709

Xie, J.-H., & Vanneste, J. (2015). A generalised-Lagrangian-mean model of the interactions between near-inertial waves and mean flow. *Journal of Fluid Mechanics*, *774*, 143–169. https://doi.org/10.1017/jfm.2015.251

Yadidya, B., Arbic, B. K., Shriver, J. F., Nelson, A. D., Zaron, E. D., Buijsman, M. C., & Thakur, R. (2024). Phase-accurate internal tides in a global ocean forecast model: Potential applications for Aadir and wide-swath altimetry. *Geophysical Research Letters*, *51*(4). https://doi.org/10.1029/2023GL107232

Yoo, J. G., Kim, S. Y., & Kim, H. S. (2018). Spectral descriptions of submesoscale surface circulation in a coastal region. *Journal of Geophysical Research: Oceans*, *123*(6), 4224–4249. https://doi.org/10.1029/2016JC012517

Zaron, E. D. (2019). Baroclinic tidal sea level from exact-repeat mission altimetry. *Journal of Physical Oceanography*, *49*(1), 193–210. https://doi.org/10.1175/JPO-D-18-0127.1

Zeitlin, V. (2018). *Geophysical fluid dynamics: Understanding (almost) everything with rotating shallow water models*. Oxford University Press.

Zhang, Z., Miao, M., Qiu, B., Tian, J., Jing, Z., Chen, G., et al. (2024). Submesoscale eddies detected by SWOT and moored observations in the Northwestern Pacific. *Geophysical Research Letters*, *51*(15), 1–9. https://doi.org/10.1029/2024GL110000

Zhao, Z. (2017). The global mode-1 S_2 internal tide. *Journal of Geophysical Research: Oceans*, *122*(11), 8794–8812. https://doi.org/10.1002/2017JC013112

Zhao, Z., Alford, M. H., Girton, J. B., Rainville, L., & Simmons, H. L. (2016). Global observations of open-ocean mode-1 M_2 internal tides. *Journal of Physical Oceanography*, *46*(6), 1657–1684. https://doi.org/10.1175/JPO-D-15-0105.1

References From the Supporting Information

Arbic, B. K., Müller, M., Richman, J. G., Shriver, J. F., Morten, A. J., Scott, R. B., et al. (2014). Geostrophic turbulence in the frequency–wavenumber domain: Eddy-driven low-frequency variability. *Journal of Physical Oceanography*, *44*(8), 2050–2069. https://doi.org/10.1175/jpo-d-13-054.1

Smith, J. A. (2008). Vorticity and divergence of surface velocities near shore. *Journal of Physical Oceanography*, *38*(7), 1450–1468. https://doi.org/10.1175/2007JPO3865.1

Torres, H. S., Klein, P., Siegelman, L., Qiu, B., Chen, S., Ubelmann, C., et al. (2019). Diagnosing ocean-wave-turbulence interactions from space. *Geophysical Research Letters*, *46*(15), 8933–8942. https://doi.org/10.1029/2019GL083675